Anisotropic Electronic Correlations in the Spin Density Wave State of La3Ni2O7

Ge He

ge.he@bit.edu.cn

Beijing Institute of Technology https://orcid.org/0000-0002-5181-4923

Jun Shen

Beijing Institute of Technology

Shiyu Xie

University of Science and Technology of China

Haotian Zhang

Beijing Institute of Technology

Mengwu Huo

Sun Yat-Sen University

Jun Shu

Wuhan University of Science and Technology https://orcid.org/0009-0005-0011-7334

Deyuan Hu

Sun Yat-Sen University

Xiaoxiang Zhou

Hefei National Laboratory

Yanmin Zhang

Lei Qin

Beijing Information Science and Technology University

Liangxin Qiao

University of Science and Technology of China

Hengjie Liu

University of Science and Technology of China

Chuansheng Hu

University of Science and Technology of China

Xijie Dong

Wuhan University of Science and Technology

Dengjing Wang

Wuhan University of Science and Technology

Jun Liu

Beijing Institute of Technology

Wei Hu
Beijing National Laboratory for Condensed Matter Physics and Institute of Physics, Chinese Academy of Sciences, Beijing 100190, China
Jie Yuan
Institute of Physics, The Chinese Academy of Sciences, Beijing National Laboratory for Condensed Matter Physics
Ya-Jun Yan
University of Science and Technology of China https://orcid.org/0000-0002-1322-0139
Zeming Qi
University of Science and Technology of China
Kui Jin
Songshan Lake Materials Laboratory https://orcid.org/0000-0003-2208-8501
Zengyi Du
Brookhaven National Laboratory https://orcid.org/0000-0003-3189-0301
Meng Wang
School of Physics, Sun Yat-Sen University https://orcid.org/0000-0002-8232-2331
Donglai Feng
Hefei National Laboratory

Article

Keywords:

Posted Date: August 5th, 2025

DOI: https://doi.org/10.21203/rs.3.rs-6952484/v1

Additional Declarations: There is **NO** Competing Interest.

Anisotropic Electronic Correlations in the Spin Density Wave State of $La_3Ni_2O_7$

Ge He[1,10]✉, Jun Shen[1]✉, Shiyu Xie[2,10], Haotian Zhang[1], Mengwu Huo[3], Jun Shu[4], Deyuan Hu[3], Xiaoxiang Zhou[5], Yanmin Zhang[6], Lei Qin[6], Liangxin Qiao[2], Hengjie Liu[2], Chuansheng Hu[2], Xijie Dong[4], Dengjing Wang[4], Jun Liu[1], Wei Hu[7], Jie Yuan[7,8], Yajun Yan[5], Zeming Qi[2], Kui Jin[7,8,9], Zengyi Du[5]✉, Meng Wang[3], Donglai Feng[5]✉

[1] *School of Mechanical Engineering, Beijing Institute of Technology, Beijing 100081, China*

[2] *National Synchrotron Radiation Laboratory, University of Science and Technology of China, Hefei, Anhui 230029, China*

[3] *Center for Neutron Science and Technology, Guangdong Provincial Key Laboratory of Magnetoelectric Physics and Devices, School of Physics, Sun Yat-Sen University, Guangzhou 510275, China*

[4] *Department of Applied Physics, Wuhan University of Science and Technology, Wuhan 430081, China*

[5] *Hefei National Laboratory, and New Cornerstone Science Laboratory, Hefei, Anhui 230088, China*

[6] *Beijing Key Laboratory for Sensor, Beijing Information Science and Technology University, Beijing 100192, China*

[7] *Beijing National Laboratory for Condensed Matter Physics, Institute of Physics, Chinese Academy of Sciences, Beijing 100190, China*

[8] *School of Physical Sciences, University of Chinese Academy of Sciences, Beijing 100049, China*

[9] *Songshan Lake Materials Laboratory, Dongguan, Guangdong 523808, China*

[10] *These authors contributed equally: Ge He and Shiyu Xie*

✉ *e-mail: ge.he@bit.edu.cn; jshen@bit.edu.cn; duzengyi@hfnl.cn; dlfeng@hfnl.cn*

ABSTRACT

The bilayer nickelate superconductor $La_3Ni_2O_7$ undergoes a density wave transition near 150 K that has attracted intensive scrutiny, yet its microscopic origin remains elusive. Here we report polarization-resolved electronic Raman scattering measurements on high-quality single crystals of $La_3Ni_2O_7$. Below 150 K, we observe a pronounced, symmetry-dependent redistribution of spectral weight in B_{1g} and B_{2g} channels, consistent with the formation of spin-density wave (SDW) gaps. Quantitative analysis reveals momentum-selective SDW gap amplitudes, with intermediate-to-strong coupling on the pockets centered at ($\pm\pi/2$, $\pm\pi/2$) and weaker coupling at ($\pm\pi$, 0) and (0, $\pm\pi$), pointing to an unconventional SDW driven by anisotropic electronic correlations. Our results establish the electronic character of the SDW in $La_3Ni_2O_7$, and provide a microscopic foundation for understanding the emergence of high-temperature superconductivity under pressure in nickelates.

INTRODUCTION

High-temperature superconductivity is often observed in proximity to an antiferromagnetic (AFM) order, as seen in cuprates [1], iron pnictides and chalcogenides [2], and more recently, the Ruddlesden-Popper (RP) phase of nickelates [3]. This recurring association suggests that magnetism may serve as a common thread in the quest for microscopic origin of high-temperature superconductivity [4–6].

The bilayer RP phase of $La_3Ni_2O_7$ has been found to exhibit high temperature superconductivity above 77 K under high pressure [7–12]. At ambient pressure, $La_3Ni_2O_7$ exhibits density-wave (DW) like transitions near 150 K, which have been extensively studied by multiple experimental techniques [13–31]. While optical measurements, including ultrafast and infrared spectroscopy [21, 26], reported gap-opening signatures associated with DW transitions, angle resolved photoemission spectroscopy (ARPES) measurements on $La_3Ni_2O_7$ show no clear gap opening [32–35]. Resolving this experimental dichotomy between optical and ARPES observations may provide key insights into the microscopic nature of DW ordering.

Spin density wave (SDW) and charge density wave (CDW) orders have been shown to be closely intertwined [19, 28, 36] with the SDW component exhibiting a larger amplitude, as evidenced by resonant inelastic X-ray scattering (RIXS) [22], neutron scattering [24], μSR [28] and nuclear magnetic resonance (NMR) [29] experiments. Efforts to elucidate the nature of SDW in $La_3Ni_2O_7$ fall into two regimes, depending on the underlying coupling strength. In the weak coupling regime [37–42], density-wave instabilities are driven by Fermi surface nesting [32–34]. In this context, possible nesting wavevectors, denoted $\mathbf{Q}_1$ and $\mathbf{Q}_2$, are superimposed on the calculated Fermi surface as shown in Fig. 1 **a**. Consequently, SDW gaps open around the Fermi energy E_F on these nested Fermi surfaces in conjunction with the density wave transition (Fig. 1 **b**).

In the strong coupling regime, by contrast, localized spin orders are stabilized [43–50] driven by strong correlation effect and Hund's coupling [49, 51–53]. This scenario is strongly supported by RIXS measurements, which directly reveal an SDW-type magnetic excitation [22]. Notably, the dispersive magnetic excitations soften to zero energy at the wavevector $(\pi/2, \pi/2)$, indicating the formation of quasi-static spin order near $T_{\mathrm{SDW}}\approx$150 K. As a consequence, the spectral function becomes markedly incoherent in the strong-coupling regime, with the Fermi surface appearing substantially broadened across the BZ (Fig. 1 **c**), distinct from the sharp, coherent Fermi surface depicted in Fig. 1 **a**. Simultaneously, spectral weight spreads broadly across the phase space (Fig. 1 **d**), accompanied by a transfer of spectral weight between particle-like and hole-like excitations

across the Fermi level, and the emergence of partial gaps associated with the SDW transition.

Raman spectroscopy, which probes both particle–particle and particle–hole excitations at $q \to 0$, is a powerful tool for accessing electronic states across different regions of the Brillouin zone via polarization selection rules [54]. Importantly, the Raman susceptibility is sensitive to the strength of electronic interactions. In the weak-coupling regime, the Raman response typically exhibits a sharp 2Δ singularity with an extended high-energy tail (Fig. 1 **e**). In contrast, strong-coupling behavior leads to a broad continuum-like response, often lacking a distinct singularity and manifesting as a broad peak, which may or may not be symmetric (Fig. 1 **f**). To resolve the nature of SDW order in $La_3Ni_2O_7$, we performed polarization-resolved electronic Raman measurements to distinguish between weak- and strong-coupling regimes. Below the transition temperature, $T < T_{SDW}$, the Raman response of B_{1g} channel exhibits a sharp coherence peak with asymmetric lineshape. In contrast, the B_{2g} channel displays a broad, incoherent, and symmetric-like peak. The temperature dependence of both channels is closely correlated with the SDW transition at $T_{\rm SDW} \approx 150$K. Guided by Raman selection rules, we attribute gap openings on β and β' pockets, with extracted magnitudes of $\Delta_{\beta'} = 23.0$ meV, and $\Delta_{\beta} = 37.5$ meV. These correspond to gap ratios of $2\Delta_{\beta'}/k_B T_{\rm SDW} \approx 3.4$ and $2\Delta_{\beta}/k_B T_{\rm SDW} \approx 5.5$, indicative of weak and medium-to-strong coupling SDW mechanisms, respectively. Thus, these results establish Raman spectroscopy as a sensitive probe of SDW electronic nature in $La_3Ni_2O_7$ and provide critical insight into the microscopic origin of density-wave formation in this single crystal.

RESULTS

$La_3Ni_2O_7$ single crystals belong to the D_{2h} point group [7]. Factor group analysis predicts ten A_g and twelve B_{1g} phonons to be Raman-active for light polarizations within the ab-plane (see Supplementary Material A for details). We identified two A_g and three B_{1g} phonon modes, labeled $A_g^{(1)}$, $A_g^{(2)}$, and $B_{1g}^{(1)}$–$B_{1g}^{(3)}$, respectively (Fig. 2). A similar Raman spectrum of $La_3Ni_2O_7$, without polarization and temperature dependence, has been previously reported in Refs. [26, 30]. The temperature-dependent phonon frequencies and linewidths are shown in Fig. S2 of Supplementary Materials A. In addition to phonon modes, we observed broad peaks marked by green triangles, located at approximately $650\,\mathrm{cm}^{-1}$ and $370\,\mathrm{cm}^{-1}$ in the xy and $x'y'$ channels, respectively (see Fig. 2 **f** and **h**). These features originate from electronic Raman scattering.

To better understand the selection rules governing the electronic Raman response, we adopt a pseudo-tetragonal point group symmetry, D_{4h}, which yields three relevant irreducible representa-

tions: A_{1g} , B_{1g}, and B_{2g}. Note that the B_{1g} phonon modes in the D_{2h} point group correspond to the B_{2g} channel in the D_{4h} point group. The corresponding Raman vertices, which are proportional to the crystal harmonics [54, 55], are illustrated in the insets of Fig. 3. These vertices highlight the momentum-space regions where particle-hole excitations are selectively probed: A_{1g} (x^2+y^2) projects electronic states near the Brillouin zone center and corners (associated with the α and α' pockets), B_{1g} (x^2-y^2) predominantly selects the β' pockets at the X and Y points, and B_{2g} (xy) emphasizes the β pocket at the X_1 point.

Figure 3 presents the electronic Raman responses in the A_{1g} , B_{1g}, and B_{2g} channels of $La_3Ni_2O_7$ over the range 100–1000 cm^{-1} at 50 K and 160 K. The difference spectra [χ''(50 K) - χ''(160 K)] are shown as light blue curves. A clear redistribution of the the spectral weight is observed in both the B_{1g} and B_{2g} symmetries, whereas no significant redistribution is found in the A_{1g} spectra. Note that the A_{1g} spectra are extracted using a linear combination of parallel and cross configurations (see more details in Supplementary Materials B). The dips at 390 cm^{-1} and 570 cm^{-1} in the A_{1g} difference spectra arise from temperature-induced changes in phonon modes (see Fig. 3**a**). In the B_{1g} channel, an asymmetric peak with a tail at the high energy side emerges near 370 cm^{-1} at low temperature (Fig. 3**b**). In contrast, the B_{2g} channel displays a pronounced redistribution characterized by a spectral weight loss below 600 cm^{-1} and a corresponding gain between 600 and 720 cm^{-1} (Fig. 3**c**). The line shape is nearly symmetric. The temperature evolution of these electronic Raman features is discussed further in Supplementary Materials C.

To further investigate the redistribution of spectral weight, we perform a quantitative analysis of the electronic continuum, as shown in Fig. 4. The background scattering is modeled using a Drude response [54], combined with a linear term to account for stray light, surface impurities, and other extrinsic effects:

$$\chi''_{\mathrm{Drude}}(\Omega) = N_F\gamma^2\frac{\Omega\tau}{1+(\Omega\tau)^2} + c\Omega, \tag{1}$$

where N_F is the density of states at the Fermi level, γ is the scattering amplitude, $1/\tau$ is the effective scattering rate, and c is a constant.

Given the distinct lineshapes of the electronic Raman responses in the B_{1g} and B_{2g} symmetries, we adopt two different models for fitting. For asymmetric lineshapes, we use the Tsuneto-Maki (TM) function [56], which is typically applied in superconducting systems but also applicable to density-wave states [57]:

$$\chi''_{\mathrm{TM}}(\Omega) = \frac{\pi}{2}\frac{(2\Delta)^2}{\Omega\sqrt{\Omega^2-(2\Delta)^2}}, \quad \Omega > 2\Delta, \tag{2}$$

where Δ denotes the density-wave gap.

For nearly symmetric lineshapes, the inelastic Raman response is empirically modeled by a Lorentzian function:

$$\chi''_{\mathrm{Lorentz}}(\Omega) = \frac{2A}{\pi}\frac{\Gamma}{4(\Omega-\Omega_0)^2+\Gamma^2}, \tag{3}$$

where A is the resonance amplitude, Ω_0 is the resonance frequency, and Γ is the linewidth. Note that the Lorentzian function describes an isolated oscillator and does not incorporate coherence effects characteristic of superconductivity [58] or SDW transitions [59]. It is employed here purely as a phenomenological tool to extract the peak position and integrated intensity.

We fit the B_{1g} and B_{2g} spectra using $\chi'' = \chi''_{\mathrm{Drude}} + \chi''_{\mathrm{TM}}$ and $\chi'' = \chi''_{\mathrm{Drude}} + \chi''_{\mathrm{Lorentz}}$, respectively, as shown in Fig. 4**a** and **b**. The fits reproduce the experimental data well. Additional fits at various temperatures can be found in Figs. S4 and S5 of the Supplementary Materials D.

The corresponding integrated spectral weights from 0 to 1000 cm^{-1} are plotted in Fig. 4**c** and **d**. A transition temperature around 150 K is clearly identified in both symmetries. In the B_{1g} symmetry (Fig. 4**c**), the spectral weight remains nearly constant below the transition, then decreases above it. In contrast, in the B_{2g} symmetry (Fig. 4**d**), the spectral weight first increases and then decreases with rising temperature. At 50 K, a total spectral weight loss of up to 10% of the maximum intensity is observed. Unlike optical conductivity, Raman scattering does not obey a sum rule, and therefore the spectral weight loss and gain are not required to balance each other [60]. The observed transition is attributed to SDW ordering, which will be discussed in detail in the Discussion section.

Figure 4 **e** presents the spectra above 150 K in the B_{2g} symmetry. A residual intensity peaked at approximately 570 cm^{-1} is observed. Unlike the spectral weight redistribution below 150 K, where both gain and loss of the spectral weight are evident, the high-temperature behavior is characterized solely by an intensity gain. Additionally, the peak intensity gradually decreases as the temperature increases.

The temperature-dependent SDW gap is plotted in Fig. 4 **f**. The gap size at the β' pocket (from the B_{1g} spectra) is extracted directly from the fits, with a maximum value of $\Delta_{\beta'} \approx 23$ meV. In contrast, the maximum gap at the β pocket (from the B_{2g} spectra), estimated from the crossing

point between spectra measured at 50 K and at 160 K, is $\Delta_\beta \approx 37.5$ meV. These correspond to ratios of $2\Delta_{\beta'}/k_BT_{\rm SDW} \approx 3.4$ and $2\Delta_\beta/k_BT_{\rm SDW} \approx 5.5$, respectively. The lineshape of the Raman response provides key insights into the underlying SDW gap structure. The SDW gap on the β' pocket is isotropic, whereas the gap on the β pocket exhibits slight anisotropy. Notably, the temperature dependence of both gaps is significantly weaker than predicted by mean-field theory (see blue curves in Fig. 4 **f**). For comparison, the SDW gaps obtained from Infrared [21] and ultrafast optical spectroscopy [26] are also plotted in Fig. 4 **f**. These values are higher than those observed in our Raman measurements, which may be attributed to differences in probe sensitivity and/or variations in oxygen content across samples [61]. To sum up, our observation reveals two distinct SDW gaps on β and β' pockets characterized by different gap magnitudes, coupling strengths, and even gap structures. These findings underscore the anisotropic SDW nature in $La_3Ni_2O_7$.

DISCUSSION

We performed systematic Raman spectroscopy on $La_3Ni_2O_7$ at ambient pressure. First, no anomalies were observed in the phonon modes across the transition, arguing against a dominant CDW instability (see Supplementary Materials A), consistent with previous studies reporting a magnetic transition near 150 K [22, 23, 29]. Second, we detected a redistribution of spectral weight associated with the opening of an SDW gap, a characteristic feature also observed in the iron pnictide $BaFe_2As_2$ [59]. While the presence of coupled spin–charge ordering cannot be entirely excluded, our findings, together with earlier reports, indicate that SDW formation is the primary electronic instability in the normal state of $La_3Ni_2O_7$ [22].

The SDW in $La_3Ni_2O_7$ has been proposed to originate from Fermi surface nesting with a wave vector $\mathbf{Q}_1$, connecting the α and β pockets, as suggested by Wang *et al.* [38]. Alternatively, a nesting scenario involving a wave vector $\mathbf{Q}_2$, connecting the β' and β pockets, has been supported by the observation of a 'translated' β Fermi surface, consistent with scattering processes involving $\mathbf{Q}_2$. [35]. The $\mathbf{Q}_1$ scenario would imply a comparable gap opening on the α pocket, which should, in principle, be observable in the A_{1g} Raman spectra. However, this is not straightforward. Screening effects can suppress the Raman intensity of gap-related excitations, particularly in conventional metals [54]. If the screening is negligible, as observed in $Ba_{1-x}K_xFe_2As_2$ [62], then the absence of gap signatures in the A_{1g} spectra would argue against the nesting vector $\mathbf{Q}_1$.

In contrast, the observed gap features in the B_{1g} and B_{2g} spectra may support wavevector $\mathbf{Q}_2$,

connecting the β' and β pockets. The distinct spectral lineshape and different $2\Delta/k_BT_{\rm DW}$ ratio, however, indicate an unconventional SDW microscopic mechanism in $La_3Ni_2O_7$. Specifically, the gap associated with the β' pocket exhibits weak coupling, while the β pocket shows a medium-to-strong coupling strength. Such strong coupling can lead to incoherency of the bands, and partial gap opening over a large momentum space in ARPES measurements, instead of clean leading-edge gap, as reported in 2H-Na_xTaS_2 [63] and $NbSe_2$ [64]. This may account for the absence of a well-defined gap in ARPES measurements [32–35]. However, the weak-coupling gap on the β' pocket, which should in principle be observable by ARPES, has not yet been detected. This discrepancy may stem from the differing sensitivities of the probes. Raman spectroscopy is bulk-sensitive, whereas ARPES primarily probes the surface, potentially leading to divergent observations. The variation in coupling strengths across different pockets suggests the presence of anisotropic coherency of the quasiparticles in $La_3Ni_2O_7$, a phenomenon widely reported in Fe-based superconductors [65, 66] and often attributed to strong Hund's coupling effects involving multiple orbitals.

Moreover, a residual peak centered at approximately 570 cm^{-1} is observed in the B_{2g} spectrum above $T_{\rm SDW}$, whose intensity gradually decreases with increasing temperature. This feature reflects a characteristic energy scale of about 70 meV in $La_3Ni_2O_7$, potentially indicating the presence of short-range magnetic order or Lorentz-type spin fluctuations. Consistent with this interpretation, RIXS measurements report that the magnon coherence length remains finite (5–10 nm) above $T_{\rm SDW}$ and diminishes gradually with increasing temperature [22]. Additionally, the deviation of the gap's temperature dependence from mean-field behavior further highlights the unconventional nature of the SDW gaps, possibly indicating the presence of spin fluctuations above $T_{\rm SDW}$ [67].

Recent μSR experiments have reported that the SDW order in $La_3Ni_2O_7$ is enhanced under increasing pressure [28]. This finding highlights the importance of exploring the pressure dependence of the electronic Raman response. High-pressure Raman measurements would directly track the evolution of the SDW gaps, offering a valuable spectroscopic probe of the underlying electronic structure changes. Such investigations could provide critical insights into the interplay between magnetism and superconductivity in high-T_c nickelate superconductors, potentially uncovering key mechanisms that drive the emergence of superconductivity in these complex materials.

Methods

Samples: High-quality $La_3Ni_2O_7$ single crystals were synthesized using a vertical optical-image floating zone technique. The growth process was conducted under an oxygen pressure of 15 bar, utilizing a 5 kW Xenon arc lamp. The samples were mechanically cleaved to obtain a flat surface

for the measurements.

Light scattering: The inelastic light scattering experiments were performed in a confocal geometry. The samples were mounted on the cold finger of a commercial Stirling fridge (ColdStation-50, MultiFields Tech.), allowing for temperature variation from 50 K to 350 K. A solid-state laser emitting at 532 nm was used. In our experiments, the laser power was set at $P = 3.0$ mW, resulting in a heating rate of $\sim$1 K/mW. We present the Raman susceptibilities $R\chi''(\Omega, T) = \pi\{1 + n(\Omega, T)\}^{-1} S(q \approx 0, \Omega)$ where R is an experimental constant, χ'' is the imaginary part of Raman response function, $S(q \approx 0, \Omega)$ is the dynamical structure factor that is proportional to the rate of scattered photons, and $n(\Omega, T)$ is the Bose-Einstein distribution function [54]. To achieve high energy resolution for the phonon lines, we used a grating with 1800 g/mm and a focal length of 800 mm, resulting in an energy resolution of 1.66 cm^{-1} . For measurements of the electronic continuum, we used a grating with 600 g/mm, achieving an energy resolution of 5.90 cm^{-1} to enhance the Raman intensity.

Data Availability

All relevant data that support the findings of this study are presented in the manuscript and supplementary information file. All data are available upon reasonable request from the corresponding authors.

[1] B. Keimer, S. A. Kivelson, M. R. Norman, S. Uchida, and J. Zaanen, From quantum matter to high-temperature superconductivity in copper oxides, Nature **518**, 179 (2015).

[2] P. Dai, Antiferromagnetic order and spin dynamics in iron-based superconductors, Rev. Mod. Phys. **87**, 855 (2015).

[3] M. Wang, H.-H. Wen, T. Wu, D.-X. Yao, and T. Xiang, Normal and superconducting properties of $La_3Ni_2O_7$, Chin. Phys. Lett. **41**, 077402 (2024).

[4] N. P. Armitage, P. Fournier, and R. L. Greene, Progress and perspectives on electron-doped cuprates, Rev. Mod. Phys. **82**, 2421 (2010).

[5] S. A. Kivelson, I. P. Bindloss, E. Fradkin, V. Oganesyan, J. M. Tranquada, A. Kapitulnik, and C. Howald, How to detect fluctuating stripes in the high-temperature superconductors, Rev. Mod. Phys. **75**, 1201 (2003).

[6] D. J. Scalapino, A common thread: The pairing interaction for unconventional superconductors, Rev. Mod. Phys. **84**, 1383 (2012).

[7] H. Sun, M. Huo, X. Hu, J. Li, Z. Liu, Y. Han, L. Tang, Z. Mao, P. Yang, B. Wang, J. Cheng, D.-X. Yao, G.-M. Zhang, and M. Wang, Signatures of superconductivity near 80 K in a nickelate under high pressure, Nature **621**, 493 (2023).

[8] Y. Zhang, D. Su, Y. Huang, Z. Shan, H. Sun, M. Huo, K. Ye, J. Zhang, Z. Yang, Y. Xu, Y. Su, R. Li, M. Smidman, M. Wang, L. Jiao, and H. Yuan, High-temperature superconductivity with zero resistance and strange-metal behaviour in $La_3Ni_2O_{7-\delta}$, Nat. Phys. **20**, 1269 (2024).

[9] N. Wang, G. Wang, X. Shen, J. Hou, J. Luo, X. Ma, H. Yang, L. Shi, J. Dou, J. Feng, J. Yang, Y. Shi, Z. Ren, H. Ma, P. Yang, Z. Liu, Y. Liu, H. Zhang, X. Dong, Y. Wang, K. Jiang, J. Hu, S. Nagasaki, K. Kitagawa, S. Calder, J. Yan, J. Sun, B. Wang, R. Zhou, Y. Uwatoko, and J. Cheng, Bulk High-temperature superconductivity in pressurized tetragonal $La_2PrNi_2O_7$, Nature **634**, 579 (2024).

[10] Y. Zhu, D. Peng, E. Zhang, B. Pan, X. Chen, L. Chen, H. Ren, F. Liu, Y. Hao, N. Li, Z. Xing, F. Lan, J. Han, J. Wang, D. Jia, H. Wo, Y. Gu, Y. Gu, L. Ji, W. Wang, H. Gou, Y. Shen, T. Ying, X. Chen, W. Yang, H. Cao, C. Zheng, Q. Zeng, J. gang Guo, and J. Zhao, Superconductivity in pressurized trilayer $La_4Ni_3O_{10-\delta}$ single crystals, Nature **631**, 531 (2024).

[11] M. Shi, D. Peng, Y. Li, Z. Xing, Y. Wang, K. Fan, H. Li, R. Wu, Z. Zeng, Q. Zeng, J. Ying, T. Wu, and X. Chen, Prerequisite of superconductivity: SDW rather than tetragonal structure in double-layer $La_3Ni_2O_{7-x}$, arXiv.2501.14202 (2025).

[12] F. Li, D. Peng, J. Dou, N. Guo, L. Ma, C. Liu, L. Wang, Y. Zhang, J. Luo, J. Yang, J. Zhang, W. Cai, J. Cheng, Q. Zheng, R. Zhou, Q. Zeng, X. Tao, and J. Zhang, Ambient pressure growth of bilayer nickelate single crystals with superconductivity over 90 K under high pressure, arXiv.2501.14584 (2025).

[13] K. Sreedhar, M. McElfresh, D. Perry, D. S. Kim, P. Metcalf, and J. Honig, Low-Temperature electronic properties of the $La_{n+1}Ni_2O_7$ (n = 2, 3, and ∞) system: Evidence for a crossover from fluctuating-valence to fermi-liquid-like behavior, J. Solid State Chem. **110**, 208 (1994).

[14] Z. Zhang, M. Greenblatt, and J. Goodenough, Synthesis, structure, and properties of the layered perovskite $La_3Ni_2O_{7-\delta}$, J. Solid State Chem. **108**, 402 (1994).

[15] S. Taniguchi, T. Nishikawa, Y. Yasui, Y. Kobayashi, J. Takeda, S. Shamoto, and M. Sato, Transport, magnetic and thermal properties of $La_3Ni_2O_{7-\delta}$, J. Phys. Soc. Jpn. **64**, 1644 (1995).

[16] Y. Kobayashi, S. Taniguchi, M. Kasai, M. Sato, T. Nishioka, and M. Kontani, Transport and magnetic properties of $La_3Ni_2O_{7-\delta}$ and $La_4Ni_3O_{10-\delta}$, J. Phys. Soc. Jpn. **65**, 3978 (1996).

[17] C. D. Ling, D. N. Argyriou, G. Wu, and J. Neumeier, Neutron diffraction study of $La_3Ni_2O_7$: Structural relationships among n=1, 2, and 3 phases $La_{n+1}Ni_nO_{3n+1}$, J. Solid State Chem. **152**, 517 (2000).

[18] G. Wu, J. J. Neumeier, and M. F. Hundley, Magnetic susceptibility, heat capacity, and pressure dependence of the electrical resistivity of $La_3Ni_2O_7$ and $La_4Ni_3O_{10}$, Phys. Rev. B **63**, 245120 (2001).

[19] Z. Liu, H. Sun, M. Huo, X. Ma, Y. Ji, E. Yi, L. Li, H. Liu, J. Yu, Z. Zhang, Z. Chen, F. Liang, H. Dong, H. Guo, D. Zhong, B. Shen, S. Li, and M. Wang, Evidence for charge and spin density waves in single crystals of $La_3Ni_2O_7$ and $La_3Ni_2O_6$, Sci. China Phys. Mech. Astron. **66**, 217411 (2022).

[20] J. Zhang, D. Phelan, A. S. Botana, Y.-S. Chen, H. Zheng, M. Krogstad, S. G. Wang, Y. Qiu, J. A. Rodriguez-Rivera, R. Osborn, S. Rosenkranz, M. R. Norman, and J. F. Mitchell, Intertwined density waves in a metallic nickelate, Nat. Commun. **11**, 6003 (2020).

[21] Z. Liu, M. Huo, J. Li, Q. Li, Y. Liu, Y. Dai, X. Zhou, J. Hao, Y. Lu, M. Wang, and H.-H. Wen, Electronic correlations and partial gap in the bilayer nickelate $La_3Ni_2O_7$, Nat. Commun. **15**, 7570 (2024).

[22] X. Chen, J. Choi, Z. Jiang, J. Mei, K. Jiang, J. Li, S. Agrestini, M. Garcia-Fernandez, H. Sun, X. Huang, D. Shen, M. Wang, J. Hu, Y. Lu, K.-J. Zhou, and D. Feng, Electronic and magnetic excitations in $La_3Ni_2O_7$, Nat. Commun. **15**, 9597 (2024).

[23] K. Chen, X. Liu, J. Jiao, M. Zou, C. Jiang, X. Li, Y. Luo, Q. Wu, N. Zhang, Y. Guo, and L. Shu, Evidence of spin density waves in $La_3Ni_2O_{7-\delta}$, Phys. Rev. Lett. **132**, 256503 (2024).

[24] T. Xie, M. Huo, X. Ni, F. Shen, X. Huang, H. Sun, H. C. Walker, D. Adroja, D. Yu, B. Shen, L. He, K. Cao, and M. Wang, Strong interlayer magnetic exchange coupling in $La_3Ni_2O_{7-\delta}$ revealed by inelastic neutron scattering, Sci. Bull. **69**, 3221 (2024).

[25] N. K. Gupta, R. Gong, Y. Wu, M. Kang, C. T. Parzyck, B. Z. Gregory, N. Costa, R. Sutarto, S. Sarker, A. Singer, D. G. Schlom, K. M. Shen, and D. G. Hawthorn, Anisotropic spin stripe domains in bilayer $La_3Ni_2O_7$, arXiv.2409.03210 (2024).

[26] Y. Meng, Y. Yang, H. Sun, S. Zhang, J. Luo, L. Chen, X. Ma, M. Wang, F. Hong, X. Wang, and X. Yu, Density-wave-like gap evolution in $La_3Ni_2O_7$ under high pressure revealed by ultrafast optical spectroscopy, Nat. Commun. **15**, 10408 (2024).

[27] M. Kakoi, T. Oi, Y. Ohshita, M. Yashima, K. Kuroki, T. Kato, H. Takahashi, S. Ishiwata, Y. Adachi, N. Hatada, T. Uda, and H. Mukuda, Multiband metallic ground state in multilayered nickelates $La_3Ni_2O_7$ and $La_4Ni_3O_{10}$ probed by 139La-NMR at ambient pressure, J. Phys. Soc. Jpn. **93**, 053702 (2024).

[28] R. Khasanov, T. J. Hicken, D. J. Gawryluk, V. Sazgari, I. Plokhikh, L. P. Sorel, M. Bartkowiak, S. Bötzel, F. Lechermann, I. M. Eremin, H. Luetkens, and Z. Guguchia, Pressure-enhanced splitting of density wave transitions in $La_3Ni_2O_{7-\delta}$, Nat. Phys. **21**, 430 (2025).

[29] D. Zhao, Y. Zhou, M. Huo, Y. Wang, L. Nie, Y. Yang, J. Ying, M. Wang, T. Wu, and X. Chen, Pressure-enhanced spin-density-wave transition in double-layer nickelate $La_3Ni_2O_{7-\delta}$, Sci. Bull. (2025).

[30] Y. Li, Y. Cao, L. Liu, P. Peng, H. Lin, C. Pei, M. Zhang, H. Wu, X. Du, W. Zhao, K. Zhai, X. Zhang, J. Zhao, M. Lin, P. Tan, Y. Qi, G. Li, H. Guo, L. Yang, and L. Yang, Distinct ultrafast dynamics of bilayer and trilayer nickelate superconductors regarding the density-wave-like transitions, Sci. Bull. **70**, 180 (2025).

[31] I. Plokhikh, T. J. Hicken, L. Keller, V. Pomjakushin, S. H. Moody, P. Foury-Leylekian, J. J. Krieger, H. Luetkens, Z. Guguchia, R. Khasanov, and D. J. Gawryluk, Unraveling spin density wave order in layered nickelates $La_3Ni_2O_7$ and $La_2PrNi_2O_7$ and via neutron diffraction, arXiv.2503.05287 (2025).

[32] J. Yang, H. Sun, X. Hu, Y. Xie, T. Miao, H. Luo, H. Chen, B. Liang, W. Zhu, G. Qu, C.-Q. Chen,

M. Huo, Y. Huang, S. Zhang, F. Zhang, F. Yang, Z. Wang, Q. Peng, H. Mao, G. Liu, Z. Xu, T. Qian, D.-X. Yao, M. Wang, L. Zhao, and X. J. Zhou, Orbital-dependent electron correlation in double-layer nickelate $La_3Ni_2O_7$, Nat. Commun. **15**, 4373 (2024).

[33] Y. Li, X. Du, Y. Cao, C. Pei, M. Zhang, W. Zhao, K. Zhai, R. Xu, Z. Liu, Z. Li, J. Zhao, G. Li, Y. Qi, H. Guo, Y. Chen, and L. Yang, Electronic correlation and pseudogap-like behavior of high-temperature superconductor $La_3Ni_2O_7$, Chin. Phys. Lett. **41**, 087402 (2024).

[34] S. Abadi, K.-J. Xu, E. G. Lomeli, P. Puphal, M. Isobe, Y. Zhong, A. V. Fedorov, S.-K. Mo, M. Hashimoto, D.-H. Lu, B. Moritz, B. Keimer, T. P. Devereaux, M. Hepting, and Z.-X. Shen, Electronic structure of the alternating monolayer-trilayer phase of $La_3Ni_2O_7$, Phys. Rev. Lett. **134**, 126001 (2025).

[35] C. C. Au-Yeung, X. Chen, S. Smit, M. Bluschke, V. Zimmermann, M. Michiardi, P. Moen, J. Kraan, C. S. B. Pang, C. T. Suen, S. Zhdanovich, M. Zonno, S. Gorovikov, Y. Liu, G. Levy, I. S. Elfimov, M. Berciu, G. A. Sawatzky, J. F. Mitchell, , and A. Damascelli, Universal electronic structure of layered nickelates via oxygen-centered planar orbitals, arXiv.2502.20450 (2025).

[36] J. Luo, J. Feng, G. Wang, N. N. Wang, J. Dou, A. F. Fang, J. Yang, J. G. Cheng, G.-q. Zheng, and R. Zhou, Microscopic evidence of charge- and spin-density waves in $La_3Ni_2O_{7-\delta}$ revealed by $^{139}La-$ NQR, Chin. Phys. Lett. (2025).

[37] D.-K. Seo, W. Liang, M.-H. Whangbo, Z. Zhang, and M. Greenblatt, Electronic band structure and madelung potential study of the nickelates La_2NiO_4, $La_3Ni_2O_7$, and $La_4Ni_3O_{10}$, Inorg. Chem. **35**, 6396 (1996).

[38] Y. Wang, K. Jiang, Z. Wang, F.-C. Zhang, and J. Hu, Electronic and magnetic structures of bilayer $La_3Ni_2O_7$ at ambient pressure, Phys. Rev. B **110**, 205122 (2024).

[39] Y. Zhang, L.-F. Lin, A. Moreo, T. A. Maier, and E. Dagotto, Structural phase transition, s-wave pairing, and magnetic stripe order in bilayered superconductor $La_3Ni_2O_7$ under pressure, Nat. Commun. **15**, 2470 (2024).

[40] F. Lechermann, S. Bötzel, and I. M. Eremin, Electronic instability, layer selectivity, and fermi arcs in $La_3Ni_2O_7$, Phys. Rev. Mater. **8**, 074802 (2024).

[41] Y.-B. Liu, J.-W. Mei, F. Ye, W.-Q. Chen, and F. Yang, s-wave pairing and the destructive role of apical-oxygen deficiencies in $La_3Ni_2O_7$ under pressure, Phys. Rev. Lett. **131**, 236002 (2023).

[42] Z. Ouyang, M. Gao, and Z. Zhongyi Lu, Absence of electron-phonon coupling superconductivity in the bilayer phase of $La_3Ni_2O_7$ under pressure, npj Quantum Mater. **9**, 80 (2024).

[43] Z. Luo, X. Hu, M. Wang, W. Wú, and D.-X. Yao, Bilayer two-orbital model of $La_3Ni_2O_7$ under pressure, Phys. Rev. Lett. **131**, 126001 (2023).

[44] Y. Zhang, L.-F. Lin, A. Moreo, and E. Dagotto, Electronic structure, dimer physics, orbital-selective behavior, and magnetic tendencies in the bilayer nickelate superconductor $La_3Ni_2O_7$ under pressure, Phys. Rev. B **108**, L180510 (2023).

[45] Y. Gu, C. Le, Z. Yang, X. Wu, and J. Hu, Effective model and pairing tendency in the bilayer Ni-based

superconductor $La_3Ni_2O_7$, Phys. Rev. B **111**, 174506 (2025).

[46] Q.-G. Yang, D. Wang, and Q.-H. Wang, Possible s-wave superconductivity in $La_3Ni_2O_7$, Phys. Rev. B **108**, L140505 (2023).

[47] C. Lu, Z. Pan, F. Yang, and C. Wu, Interlayer-coupling-driven high-temperature superconductivity in $La_3Ni_2O_7$ under pressure, Phys. Rev. Lett. **132**, 146002 (2024).

[48] X.-Z. Qu, D.-W. Qu, J. Chen, C. Wu, F. Yang, W. Li, and G. Su, Bilayer $t-J-J_\perp$ model and magnetically mediated pairing in the pressurized nickelate $La_3Ni_2O_7$, Phys. Rev. Lett. **132**, 036502 (2024).

[49] Y. Cao and Y. Yang, Flat bands promoted by hund's rule coupling in the candidate double-layer High-temperature superconductor $La_3Ni_2O_7$ under high pressure, Phys. Rev. B **109**, L081105 (2024).

[50] J. Chen, F. Yang, and W. Li, Orbital-selective superconductivity in the pressurized bilayer nickelate $La_3Ni_2O_7$: An infinite projected entangled-pair state study, Phys. Rev. B **110**, L041111 (2024).

[51] V. Christiansson, F. Petocchi, and P. Werner, Correlated electronic structure of $La_3Ni_2O_7$ under pressure, Phys. Rev. Lett. **131**, 206501 (2023).

[52] Y.-H. Tian, Y. Chen, J.-M. Wang, R.-Q. He, and Z.-Y. Lu, Correlation effects and concomitant two-orbital s-wave superconductivity in $La_3Ni_2O_7$ under high pressure, Phys. Rev. B **109**, 165154 (2024).

[53] U. Kumar, C. Melnick, and G. Kotliar, Softening of dd excitation in the resonant inelastic X-ray scattering spectra as a signature of hund's coupling in nickelates, Phys. Rev. Res. **7**, L012066 (2025).

[54] T. P. Devereaux and R. Hackl, Inelastic light scattering from correlated electrons, Rev. Mod. Phys. **79**, 175 (2007).

[55] S. Djurdjić Mijin, A. Baum, J. Bekaert, A. Šolajić, J. Pešić, Y. Liu, G. He, M. V. Milošević, C. Petrovic, Z. V. Popović, R. Hackl, and N. Lazarević, Probing charge density wave phases and the mott transition in $1T-TaS_2$ by inelastic light scattering, Phys. Rev. B **103**, 245133 (2021).

[56] T. Tsuneto, Transverse collective excitations in superconductors and electromagnetic absorption, Phys. Rev. **118**, 1029 (1960).

[57] N. Lazarević and R. Hackl, Fluctuations and pairing in Fe-based superconductors: light scattering experiments, J. Phys.: Condens. Matter **32**, 413001 (2020).

[58] G. He, D. Li, D. Jost, A. Baum, P. P. Shen, X. L. Dong, Z. X. Zhao, and R. Hackl, Raman study of cooper pairing instabilities in $(Li_{1-x}Fe_x)OHFeSe$, Phys. Rev. Lett. **125**, 217002 (2020).

[59] L. Chauvière, Y. Gallais, M. Cazayous, M. A. Méasson, A. Sacuto, D. Colson, and A. Forget, Raman scattering study of spin-density-wave order and electron-phonon coupling in $Ba(Fe_{1-x}Co_x)_2As_2$, Phys. Rev. B **84**, 104508 (2011).

[60] J. Kosztin and A. Zawadowski, Violation of the f-sum rule for raman scattering in metals, Solid State Commun. **78**, 1029 (1991).

[61] Z. Dong, M. Huo, J. Li, J. Li, P. Li, H. Sun, L. Gu, Y. Lu, M. Wang, Y. Wang, and Z. Chen, Visualization of oxygen vacancies and self-doped ligand holes in $La_3Ni_2O_{7-\delta}$, Nature **630**, 847 (2024).

[62] T. Böhm, A. F. Kemper, B. Moritz, F. Kretzschmar, B. Muschler, H.-M. Eiter, R. Hackl, T. P.

Devereaux, D. J. Scalapino, and H.-H. Wen, Balancing act: Evidence for a strong subdominant d-wave pairing channel in $Ba_{0.6}K_{0.4}Fe_2As_2$, Phys. Rev. X **4**, 041046 (2014).

[63] D. W. Shen, B. P. Xie, J. F. Zhao, L. X. Yang, L. Fang, J. Shi, R. H. He, D. H. Lu, H. H. Wen, and D. L. Feng, Novel mechanism of a charge density wave in a transition metal dichalcogenide, Phys. Rev. Lett. **99**, 216404 (2007).

[64] D. W. Shen, Y. Zhang, L. X. Yang, J. Wei, H. W. Ou, J. K. Dong, B. P. Xie, C. He, J. F. Zhao, B. Zhou, M. Arita, K. Shimada, H. Namatame, M. Taniguchi, J. Shi, and D. L. Feng, Primary role of the barely occupied states in the charge density wave formation of $nbse_2$, Phys. Rev. Lett. **101**, 226406 (2008).

[65] K. Haule and G. Kotliar, Coherence–incoherence crossover in the normal state of iron oxypnictides and importance of Hund's rule coupling, New J. Phys. **11**, 025021 (2009).

[66] Z. K. Liu, M. Yi, Y. Zhang, J. Hu, R. Yu, J.-X. Zhu, R.-H. He, Y. L. Chen, M. Hashimoto, R. G. Moore, S.-K. Mo, Z. Hussain, Q. Si, Z. Q. Mao, D. H. Lu, and Z.-X. Shen, Experimental observation of incoherent-coherent crossover and orbital-dependent band renormalization in iron chalcogenide superconductors, Phys. Rev. B **92**, 235138 (2015).

[67] G. Grüner, Density Waves in Solids (Perseus, Cambridge, MA, 1994).

Acknowledgments

We thank Rudi Hackl, Thomas P. Devereaux, George Sawatzky, Gheorghe Lucian Pascut and Kejin Zhou for fruitful discussions. This work is supported by the National Key Basic Research Program of China (Grants No. 2024YFF0727103, 2024YFB4007301), the National Natural Science Foundation of China (Grants No. 12474473, U23A6015, 12104490, 12375331, 52201036), Z.D. acknowledges the support by Hefei National Laboratory. D.L.F acknowledges the support by the New Cornerstone Science Foundation (Grant No. NCI202211), and the Innovation Program for Quantum Science and Technology (Grant No. 2021ZD0302803). L.Q. acknowledges the support by the Youth Beijing Scholars program (Grant No. 93) and the Project of Construction and Support for high-level Innovative Teams of Beijing Municipal Institutions (BPHR20220124). J.Y. and K.J. acknowledge the support by CAS Project for Young Scientists in Basic Research (Grant No. 2022YSBR-048). M.W. was supported by the National Natural Science Foundation of China (12425404), the Guangdong Basic and Applied Basic Research Foundation (2024B1515020040), the Guangdong Provincial Key Laboratory of Magnetoelectric Physics and Devices (2022B1212010008), and the Research Center for Magnetoelectric Physics of Guangdong Province (2024B0303390001).

Author contributions

G.H., Z.D., J.S. and D.L.F. conceived the project. G.H., S.Y.X., H.T.Z. and L.X.Q. performed the Raman measurements. C.S.H., H.J.L. and W.H. contributed to the experimental assistance. G.H., Z.D., J.S., Y.M.Z., X.X.Z., L.Q., X.J.D., D.J.W., J.L., Y.J.Y., Z.M.Q., J.Y. and K.J. analyzed the Raman data. M.W., M.W.H. and D.Y.H. synthesized and characterized the samples. G.H., Z.D. and Y.M.Z. wrote the manuscript with comments from all the authors.

Competing interests

The authors declare no competing interests.

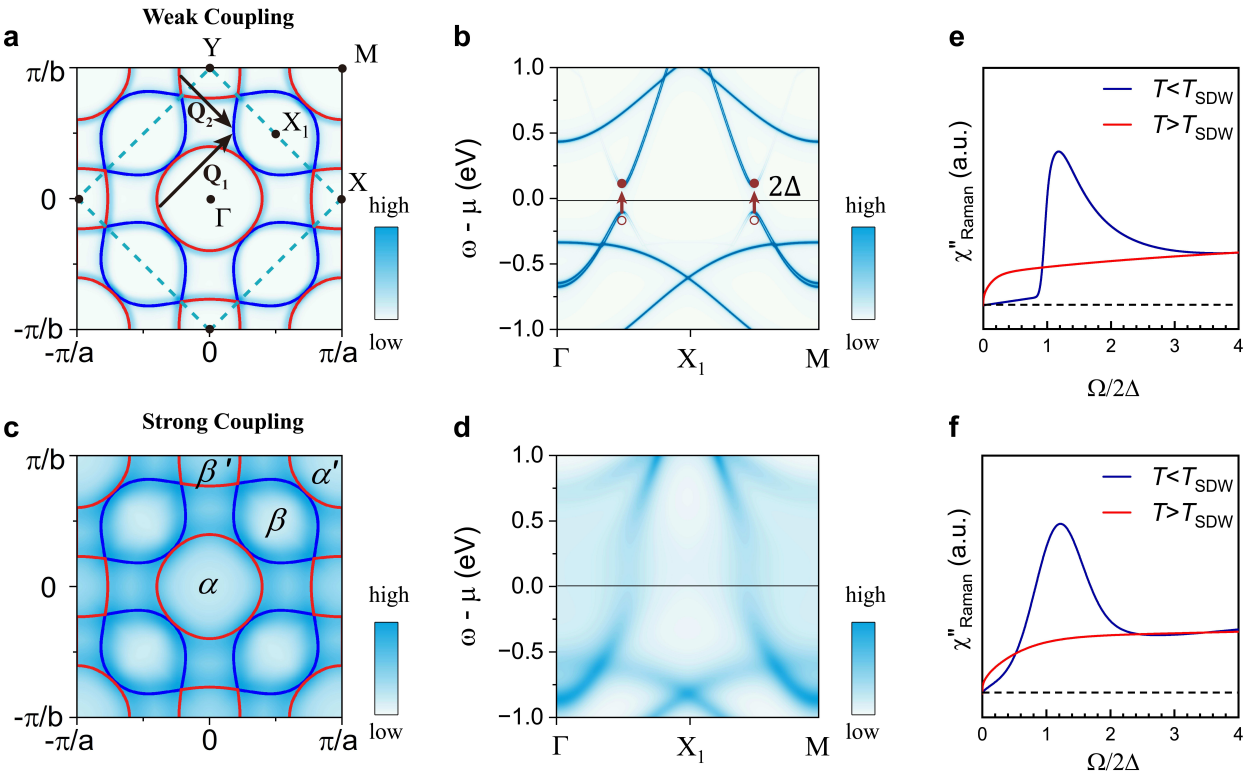

Figure 1. **Comparison of the electronic structure and Raman spectroscopic characteristics in weak and strong coupling regimes in $La_3Ni_2O_7$.** **a**, Fermi surface in the weak coupling regime, calculated using an 8-band tight-binding model (see Supplementary Materials E for details). The solid lines represent the Brillouin zone (BZ) of the ideal unit cell (without considering tilted Ni-O octahedra), while the dashed lines indicate the BZ of the real unit cell (with tilted Ni-O octahedra). The blue and red curves denote hole (β) and electron (α, β', α') pockets arising from band 3 and band 4, respectively. The black arrows indicate the wavevectors $\mathbf{Q}_1$ connecting α and β pockets and $\mathbf{Q}_2$ connecting β and β' pockets, respectively. **b**, Spectral weight $A(k,\omega)$ calculated within a mean-field approximation considering a density wave gap Δ induced by Fermi surface nesting with a specific wave vector. **c**, Fermi patches in the strong coupling regime, where strong interactions lead to a broadened distribution of electronic states near the Fermi level across the BZ. **d**, Spectral weight $A(k,\omega)$ in the strong coupling regime, where a broad continuum appears due to incoherent particle-hole mixing, allowing excitations both below and above the Fermi level, unlike the sharp features in a normal band picture. **e**, Typical Raman spectral features of an SDW system in the weak coupling regime, exhibiting well-defined coherence peaks. **f**, Example Raman spectral response of an SDW system in the strong coupling regime, characterized by a broad redistribution of spectral weight instead of sharp features.

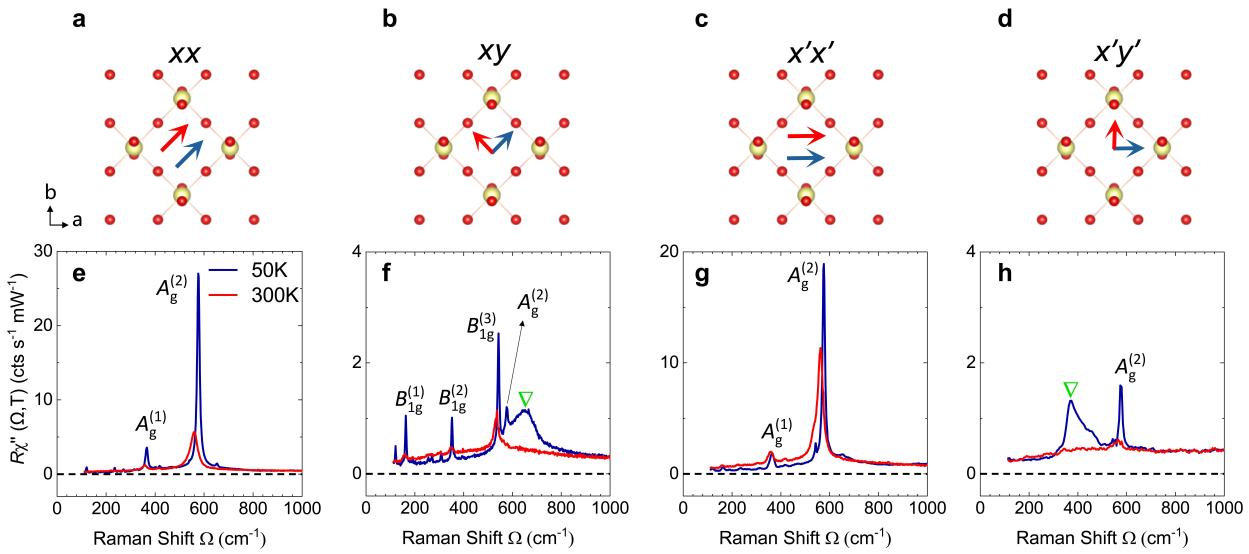

Figure 2. **Polarization configurations and corresponding Raman spectra. a**–**d**, Schematic definitions of the polarization configurations, where red and yellow spheres represent oxygen and nickel atoms, respectively. The x- and y-axes are aligned along the Ni–O–Ni bond directions. The x' and y' polarizations are rotated by 45° clockwise from the x and y axes, respectively. **e**–**h**, Raman spectra measured at 50 K and 300 K for the corresponding configurations. Raman-active phonon modes are labeled as indicated. Green triangles denote the presence of additional electronic Raman responses in the xy and $x'y'$ channels.

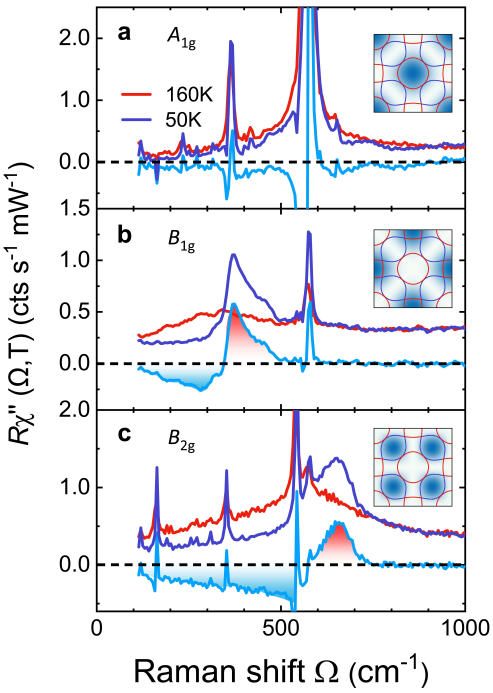

Figure 3. **Normal and SDW state Raman spectra of $La_3Ni_2O_7$ at temperatures as indicated.** The difference spectra between 50 K and 160 K are overlaid as light blue curves. Spectral weight redistribution is clearly observed in the B_{1g} and B_{2g} channels. The spectral weight loss is highlighted in blue, while the gain is indicated in red. Insets: Color maps of Raman vertices in the first BZ for the A_{1g} , B_{1g}, and B_{2g} symmetries, respectively.

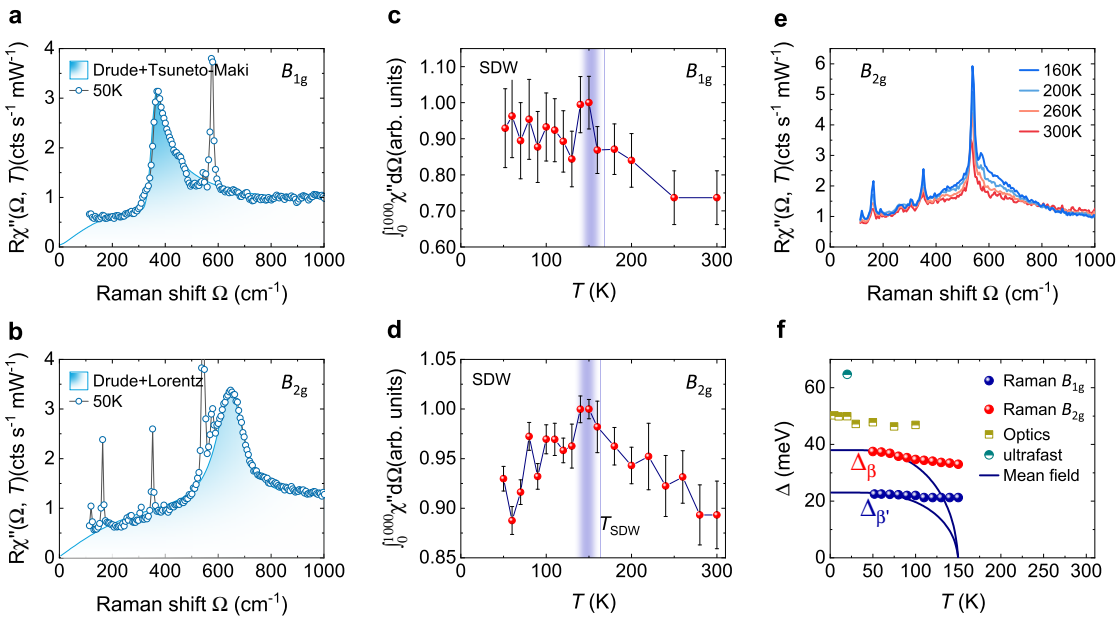

Figure 4. **Spectral weight and energy gap in $La_3Ni_2O_7$.** **a** and **b**, Fits of the electronic continuum at 50 K using phenomenological Drude–Tsuneto-Maki and Drude–Lorentz models for the B_{1g} and B_{2g} spectra, respectively. **c** and **d**, Integrated spectral weight from 0 to 1000 cm^{-1} (red solid circles) as a function of temperature in the B_{1g} and B_{2g} channels. The SDW transition temperature is marked by the light blue vertical bands. **e**, Raman response in the B_{1g} symmetry at 160 K, 200 K, 260 K, and 300 K. **f**, Temperature dependence of the SDW energy gaps. The half-filled circles and squares are adapted from ultrafast spectroscopy [26] and optical conductivity [21], respectively. Red and blue points represent the energy gaps at the β and β' pockets extracted from the Raman measurements. The deviation from the mean-field theory prediction is illustrated by the blue curves.

Supplementary Files

This is a list of supplementary files associated with this preprint. Click to download.

- SIAnisotropicElectronicCorrelationsintheSpinDensityWaveStateofLa3Ni2O7.pdf